Energy-dependent fragmentation cross sections of relativistic ^{12}C

T. Ogawa, T. Sato, S. Hashimoto, D. Satoh, and S. Tsuda
Research Group for Radiation Transport Analysis, Japan Atomic Energy Agency, Tokai, Ibaraki, Japan

K. Niita
Research Organization for Information Science and Technology, Tokai, Ibaraki, Japan

(Received 3 July 2015; revised manuscript received 22 July 2015; published 20 August 2015; publisher error corrected 25 August 2015)

The fragment production excitation functions of ^{12}C interacting with carbon nuclei were measured in the energy range of 100–400 MeV/u. To measure cross sections as excitation functions, fragments produced from a thick carbon target bombarded with a monoenergetic ^{12}C ion beam were detected by a telescope detector placed behind the target. By this measurement, eight isotopes—^{11}B, ^{10}B, ^{10}Be, ^{9}Be, ^{7}Be, ^{8}Li, ^{7}Li, and ^{6}Li—were identified, and the energy dependence of their production cross sections in the few 100 MeV/u range was obtained. Based on the measured cross sections, the JAERI quantum molecular dynamics model was updated to incorporate the mechanisms particularly important for peripheral collisions. The improved version of the model coupled with a statistical decay model reproduces the measured data typically within a few 10% of difference.

DOI: 10.1103/PhysRevC.92.024614 PACS number(s): 25.70.Mn

I. INTRODUCTION

Understanding nucleus-nucleus collisions is important for studying nuclear physics such as parameters of the nuclear equation of state [1], phase transition of nuclear matter [2], and properties of exotic nuclei [3]. In addition, from the application viewpoint, relativistic nucleus-nucleus collisions play an important role in accurate evaluation of exposure due to cosmic rays during space missions, doses in heavy-ion cancer therapy, and safety of energetic heavy-ion accelerators. In these applications, the isotopic identity of fragments and energy of heavy ions are vital because dosimetric impact and spatial distribution are dependent on charge, mass, and energy of the fragments.

Availability of fragmentation cross section data measured systematically over a wide energy range has been limited. Energy-dependent fragmentation cross sections were measured by changing beam energy [4–7] or by the stacked-foil method [8,9]. In the former method, the experimental data recorded at different energies were inconsistent at times because of various different systematic errors. Moreover, the stacked-foil method is not applicable to the fragmentation of light targets, nonradioactive fragments, or short-lived fragments.

To simulate nucleus-nucleus collisions and the resulting particle production, a quantum molecular dynamics (QMD) [10] model was developed as a microscopic reaction model [11–13]. QMD has a few degrees of freedom in its description of physics; therefore, several reaction event generators have been developed based on QMD approach. The QMD model developed by Chikazumi *et al.* [14] incorporated momentum-dependent force, surface tension, and Pauli force into the Hamiltonian as effective potential terms, and it was used for investigating multifragmentation. ImQMD (improved quantum molecular dynamics) [15] assumed that the size of nucleon wave packet depends on the system size to reproduce reactions slightly above reaction thresholds. RQMD (relativistic quantum molecular dynamics) [16] considered phenomena characteristic of high-energy reactions, such as string fusion into color ropes, to study ultrarelativistic collisions. In addition to QMD models, some cascade models such as the Dubna cascade model [17,18], the Los Alamos quark-gluon string model [19], and the Liège intranuclear cascade [20], have been developed and used to simulate nucleus-nucleus reactions. These models are used not only as stand-alone event generators but also as build-in event generators of general-purpose radiation transport simulation codes [21–27].

Analysis of fragment formation is an important aspect of nucleus-nucleus collision studies, and QMD is appropriate for simulating fragmentation. JQMD is a QMD-type reaction model that can treat fragment formation by tracking the motion of nucleons explicitly. Fragment-production cross sections determined using JQMD were benchmarked against the cross sections measured in experiments [28,29].

In general, fragment yields increase with fragment masses closer to the target/projectile mass; however, the estimation of target/projectile-like fragments using QMD-type models is difficult. Their production is particularly sensitive to the ground-state configuration and excitation energy fluctuation during time evolution, which may cause spurious disintegration.

In this study, we develop a new method to measure isotopic fragmentation cross-sections as functions of energy from about 100 to 400 MeV/u and apply it to measure fragmentation cross sections of ^{12}C($^{\mathrm{Nat}}$C,x)X reactions, the most typical reactions of light nuclei. In addition, JQMD, partly improved by Mancusi *et al.* in their earlier study [30] to describe the Hamiltonian in a Lorentz-covariant form and stabilize the ground-state nuclei (R-JQMD), was improved further based on the obtained experimental data. In this study, the in-medium effect on nucleon-nucleon scattering cross sections was corrected, and inessential assumptions that had been introduced into JQMD to overcome ground-state instability were eliminated.

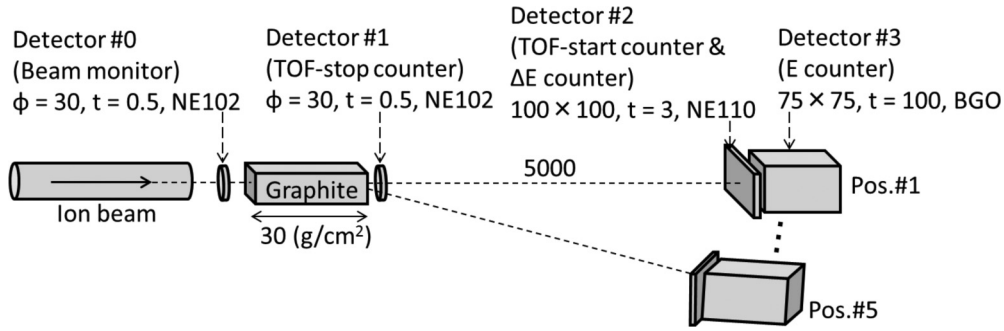

FIG. 1. Schematic diagram of experimental setup (units are mm, not to scale). Detectors 2 and 3 were moved from position ♯1 to ♯5.

Using the revised version of the model (JQMD-2.0), yield of near-projectile fragments and lighter fragments are reproduced generally better than with the old version of the model.

II. METHODS

A. Experiment

1. Principle of detection method

In nucleus-nucleus collision reactions, the spectator parts of nuclei do not directly interact with the reaction partner; therefore, their momenta are mostly conserved. Consequently, the velocity of projectile fragments is close to that of the incident nuclei, and angular distribution of fragments peaks sharply in the forward direction. Moreover, the stopping power of fragments is generally lower than that of projectiles. Accordingly, if a collimated heavy ion beam is directed at a thick target, fragments produced in the depth of the target lose a considerable amount of energy as primary ions before fragmentation and come out from the target at low velocities. In contrast, fragments produced near the incident surface lose less energy as fragments and come out at high velocities. In a thick target bombarded by monoenergetic heavy ions, the correlation between the depth of the reaction point and the kinetic energy of the fragment on the downstream surface of the target is formulated as follows:

$$l = \int_{E_r}^{E_0} \frac{1}{s_p(E)} dE + \int_{E_e}^{E_r - \delta E(E_r)} \frac{1}{s_f(E)} dE, \qquad (1)$$

where l is the target thickness, E_0 is the projectile incident energy, E_r is the projectile kinetic energy at the reaction point, $s_p(E)$ is the stopping power of the projectile, $\delta E(E_r)$ is the kinetic energy loss in the fragmentation reaction, E_e is the kinetic energy of the fragment on the downstream surface, and $s_f(E)$ is the stopping power of the fragment. The empirical parametrization developed by Tarasov *et al.* [31] was used to estimate $\delta E(E_r)$. Mean momentum loss was calculated using the formula as a function of projectile momentum, and momentum was assumed to be reduced for the same magnitude in every fragmentation reaction without statistical fluctuation. The stopping power of fragments and projectiles was calculated using SRIM [32]. By solving Eq. 1, E_t was obtained as a function of E_e. By measuring the kinetic energy of each fragment behind the target (E_e) and using Eq. (1), fragmentation cross sections as functions of energy were obtained as follows:

$$\phi\, \sigma_f(E_r) \frac{dE_r}{dz} \exp\left[-n \int_{E_r}^{E_0} \sigma_{l,p}(E) \frac{1}{s_p(E)} dE - n \int_{E_e}^{E_r - \delta E(E_r)} \sigma_{l,f}(E) \frac{1}{s_f(E)} dE \right] = \frac{dN(E_e)}{dE_e} \frac{dE_e}{dE_r} dE_r, \qquad (2)$$

where ϕ is the incident primary ion flux, σ_f is the fragmentation cross section, E_r is the energy of the fragmentation reaction, z is the depth inside the target, n is the atomic density of the target, $\sigma_{l,p}$ is the total reaction cross section of primary ions, s_p is the stopping power of projectiles, $\sigma_{l,f}$ is the total reaction cross section of fragments, s_f is the stopping power of fragments, $N(E)$ is the number of fragments with kinetic energy E behind the target, and E_e is the energy of the fragments behind the target. The exponential term represents fragment loss by nuclear reactions with the target material. The total reaction cross section was calculated using Kurotama model [33]. In addition to the kinetic energy at the reaction point, the identification of fragment mass and charge was necessary to obtain isotopic fragmentation cross sections.

2. Actual setup of detectors and associated electronics

The detection system designed to perform the above-described measurement is shown in Fig. 1. The most upstream detector served as a beam current monitor. The fragments produced in the target passed through the TOF (time-of-flight) stop counter immediately behind the target. After transmission along the 5-m-long TOF path, the fragments were detected by a 3-mm-thick scintillator, which served as both the TOF start counter and the ΔE counter, and the E counter of the thick bismuth germanate (BGO). TOF start and TOF stop were inverted to cut off noise events as explained later. Hereafter, the most upstream detector (0.5-mm-thick NE102), TOF stop counter (0.5-mm-thick NE102), TOF start counter (3-mm-thick NE110) and the most downstream detector (100-mm-thick BGO) are referred to as detectors 0, 1, 2, and 3, respectively.

The experiment was performed at the general-purpose irradiation room (PH1) of the Heavy Ion Medical Accelerator in Chiba (HIMAC) at the National Institute of Radiological Sciences (NIRS). The 400 MeV/u ^{12}C ion beam was transferred from the synchrotron through a 100-μm-thick

aluminum beam window to the target as 500-ms-long pulses with repetition intervals of 3.3 s. The beam was collimated to less than 1 cm in diameter and directed normally to the geometrical center of detector 0. The beam intensity was varied from 67 000 to 300 000 particles/pulse depending on the position of detectors 2 and 3 to keep the event rate at around 500 events/pulse. At this count rate, dead time was around 15%.

Although the projectile fragments were forward peaked, the solid angle of detector 3 (2.25×10^{-4} sr) was not sufficiently large to detect all projectile fragments. Therefore, detectors 2 and 3 were moved five steps outward, and the measurement was performed in each configuration. The measured data were finally summed up with weighting by the solid angle. Thus, fragments within the angular range of 0° to 3.86° were detected.

The length of the TOF path (the distance between detectors 1 and 2) was determined to be 5 m by comparing TOF precision and detector acceptance. Because the kinetic energy of target fragments is too low to reach the detectors, the target fragments were cut off automatically, and only projectile fragments were detected. The target had to be thick enough to stop the primary ions, otherwise output signals of detectors 2 and 3 would be dominated by the primary ions. Hence, fragments with stopping power larger than that of primary ions (e.g., ^{11}C) were not detected because they were stopped inside the target.

The thickness of detector 3 was selected to fully stop Li and heavier fragments. H and He fragments were disregarded in the measurement because more than one fragment often hits the detectors in one reaction event, in which case isotope identification is impossible. Moreover, the angular distribution of H and He fragments was so wide that the acceptance in this experiment was insufficient.

Note that in this measurement, absolute signal intensity calibration is not necessary. Detector 0 was used to count the number of incident particles. Detector 1 was used to output the TOF timing signal. Detectors 2 and 3 were used for isotope identification, and the correspondence between the data points and fragment isotopic identity was clear. Absolute time calibration was performed for TOF measurement between detectors 1 and 2.

The target with a thickness of 30.0 g/cm^2 was assembled using 5 cm × 5 cm square graphite plates with an average density of 1.82 g/cm^3 and impurities less than 0.5%. Because this thickness was slightly lower than the range of primary ions (30.7 g/cm^2), the primary ions penetrated the target with a mean exit energy of 68.75 MeV/u according to the SRIM calculation. This energy was so low that the primary ions exiting the target were stopped in detector 2 without the generation of any noise signal in detector 3. Such events were eventually cut off. The TOF path length was measured with an accuracy of a few millimeters every time detectors 2 and 3 were moved. Detector 2 and 3 may detect fragments produced in detector 1 or air in the TOF path. However, the kinetic energy of the projectile fragments produced behind the target was mostly less than 68.75 MeV/u, which is the kinetic energy of the primary ions. The kinetic energy of the projectile fragments was too low to penetrate detector 2; therefore, they did not affect the measurement.

Figure 2 shows a block diagram of the electronics for signal processing. High voltages, i.e., 1200, 1400, 1450, and 1350 V, were applied to the photomultiplier tubes (PMTs) of detectors 0, 1, 2, and 3, respectively. These voltages were optimized to increase the signal-to-noise ratio and avoid output saturation of the PMTs. Because the signal-to-noise ratio of detector 3

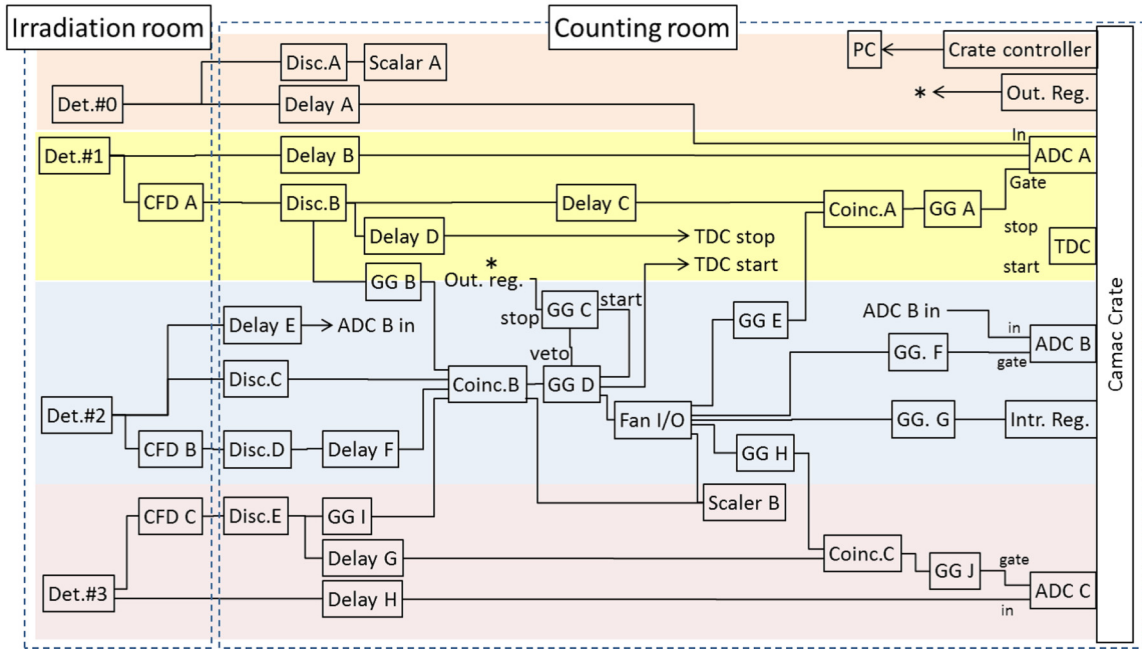

FIG. 2. (Color online) Block diagram of the signal-processing circuit. CFD: constant fraction discriminator; Disc: discriminator; Coinc: coincidence; GG: gate generator; ADC: analog-to-digital converter; TDC: time-to-digital converter; Int.Reg: interrupt register; Out.Reg: output register.

was critical in our measurement, its bias voltage was increased to 1350 V, and an attenuator was installed to avoid overflow of the analog-to-digital converter (ADC). The output signals of the detectors were fed to the ADCs, which were mounted on a computer automated measurement and control (CAMAC) crate. The pulse height spectrum of detector 0's signal was considered to estimate the probability of primary ion random coincidence. The events in which more than one primary ions hit detector 0 were disregarded in the offline analysis to exclude the random coincidence events. The time interval of the output signals of detectors 1 and 2, digitized by constant fraction discriminators (CFD), was recorded using a time-to-digital converter (TDC) mounted on the CAMAC crate. Because the CFDs were placed inside the irradiation room and output signals were attenuated during transmission from the irradiation room, discriminator modules were connected to recover signal height. The output signals of detectors 1, 2, and 3 were digitized and processed using coincidence module B to provide trigger signals to the ADCs and TDC only when detectors 1, 2, and 3 simultaneously detected meaningful energy deposition. The discrimination level of discriminator module C was adjusted to cut off events by H and He fragments. When a trigger signal was generated, gate signals long enough to fully accumulate scintillator output signals were fed to the ADCs. The output signals of coincidence module B were transmitted to gate generator D. The output of gate generator D was inhibited by gate generator C immediately after the signal output until gate generator C received the output register signal. Using this mechanism, the ADCs integrated detector output analog signals in a single event. By counting the output signals of coincidence module B and gate generator D using scaler B, dead time ratios were estimated. The lengths of the gate signals of ADCs A, B, and C were 60, 60, and 1000 ns, respectively. Independent of the trigger signal, the output signal of detector 0, digitized by discriminator A, was counted by scaler A to measure the primary ion beam intensity. The CAMAC crate was interfaced to a personal computer using the Kakuken online data acquisition system [34]. The background count rate of the beam monitor (detector 0) was considerably lower than 0.1 count/s. The background count rates of the other detectors were not observed because trigger signals were not generated unless the output signals of detectors 1, 2, and 3 coincided within a 170-ns time window. In this time window, TOF signals of the fragments with kinetic energy less than 5.8 MeV/u were cut off. Employing the inverse TOF technique, the output signals of detectors 2 and 1 were used as TDC start and stop timing signals, respectively. By using the inverse TOF technique, the TDC was activated only when energy was deposited in detectors 1, 2, and 3 coincidentally. Zero-point calibration was performed by placing detector 2 just downstream of detector 1 and excluding detector 3 from the coincidence.

3. Data processing

The digital outputs of the ADCs and TDC were analyzed ofline. To quantify reaction energy and identify charge and mass of the fragments observed in each event, the obtained data were processed according to the following four steps:

(1) Z identification,

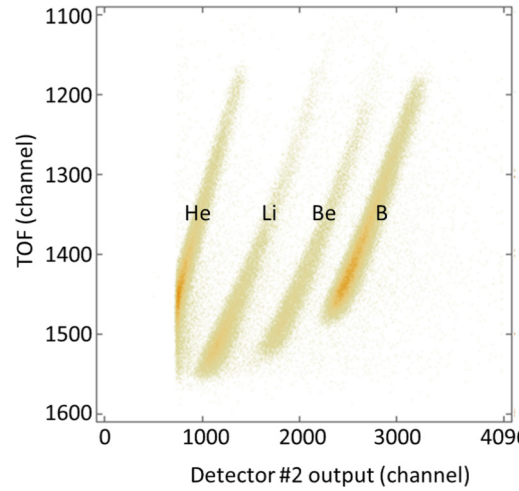

FIG. 3. (Color online) Two-dimensional distribution of detector 2 output vs TOF.

(2) A identification,
(3) conversion of TOF to outgoing energy,
(4) conversion of outgoing energy to reaction energy,

where outgoing energy is the kinetic energy of a fragment on the downstream surface of the target and reaction energy is the kinetic energy of a primary ion at the reaction point.

A typical example of fragment charge identification is shown in Fig. 3. Fragments from He to B were identified clearly in the plot. The data points were distributed diagonally in the plain owing to the fragments' energy distribution. Because the signals corresponding to H and He were cut off by the discriminator associated with detector 2, low-energy He could not be cut off. The events were classified into three groups, i.e., Li, Be, and B, and analyzed further; He events were disregarded. As suggested by the calculation using SRIM, the primary ion beam was not observed in the plot because primary ions were stopped before hitting detector 3.

As an example, fragment mass identification of Li is shown in Fig. 4. In the (detector 3 output)–(TOF) plane, the signals categorized under Li in the previous step were placed along four different curved lines corresponding to ^{9}Li, ^{8}Li, ^{7}Li, and ^{6}Li. The bent line below the ^{6}Li line corresponded to the coincidence of two ^{4}He. According to the SRIM calculation, 400 MeV/u ^{4}He penetrating the target has kinetic energy of 314 MeV/u. This energy is sufficient to penetrate the 10-cm-thick BGO; therefore, the signal distribution shape of the coincidence of two ^{4}He is reasonable. In this way, the charge and mass of fragments detected in each event were identified.

In general, TOF measured in each event can be converted to fragment kinetic energy using Eq. (3),

$$E_{\mathrm{e}} = \left(\sqrt{\frac{1}{1-\left(\frac{L}{ct}\right)^2}} - 1 \right) m_0 c^2, \tag{3}$$

where E_{e} is the kinetic energy on the target downstream surface, m_0 is the fragment rest mass, c is the speed of light, L is the TOF path length, and t is the flight time. However, in our study, to consider energy loss of fragments in the TOF

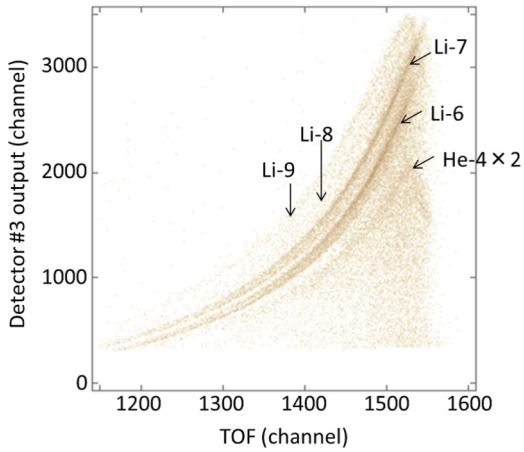

FIG. 4. (Color online) Two-dimensional distribution of detector 3 output vs TOF obtained at detection position 1 (most forward point).

path, TOF was converted using Eq. (4) as follows:

$$\beta(E_e)c\Delta t = \Delta L, \qquad E_e \rightarrow E_e - s_a \Delta L, \tag{4}$$

where ΔL is the length element along the TOF path, Δt is the corresponding time element of TOF, and s_a is the stopping power of fragments in air. By recursively solving Eq. (4) until the sum of ΔL was equal to the TOF path L, E_e was obtained as a function of TOF, which was obtained as the sum of Δt.

By combining Eqs. (1) and (4) with $E_0 = 400$ (MeV/u) and $l = 16.5$ cm, the obtained kinetic energy was converted to kinetic energy at the reaction point. $N(E_e)$ in Eq. (2) was obtained subsequently. When detectors 2 and 3 were moved from the center, target thickness t in Eq. (1) was corrected as $t/\cos(\theta)$ where θ is the angle of the detection point with respect to the beam axis. Incident primary ion flux in Eq. 2 was estimated using the number of signals counted by detector 0 with consideration for random coincidence estimated from the signal spectrum of detector 0.

By moving detectors 2 and 3, fragments emitted at emission angles less than 3.86° were measured. To consider fragments emitted at larger angles, the angular distribution of fragments, which was dominated by multiple Coulomb scattering [35] and fragmentation reaction [36], was fitted by a Gaussian function and the correction factor was evaluated as the ratio of the function integrated up to 3.86° and that integrated up to 180°. The correction factor for ^{11}B was the smallest, ranging from 1.00 to 1.03, whereas that for ^{6}Li was the largest, ranging from 1.15 to 2.44. Typical fitting of the fragment angular distribution is shown in Fig. 5.

To finally evaluate the fragmentation excitation functions, uncertainties of energy and cross sections were analyzed. The energy uncertainties were estimated considering the following components:

(1) TOF zero point,
(2) energy loss calculation by SRIM,
(3) target thickness,
(4) TOF path length,
(5) energy loss in reaction,
(6) energy straggling.

The uncertainty of the TOF zero point is attributed to photon propagation in detector 2. TOF start signal timing fluctuated within δt as follows:

$$\delta t = w/c' = 0.589 \text{ ns}, \tag{5}$$

where w is the distance between the points closest to and farthest from the photoelectric surface in the detector (0.112 m), and c' is the speed of light in the detector (1.90×10^8 m/s). According to the literature on SRIM-2010, the uncertainty in energy loss is 5.6% for ions heavier than Be [32]. The target thickness measured by weighing the mass of the target plates had an uncertainty of about 1.0%. The fluctuation of the TOF path length, measured by a laser distance meter, was less than 0.1%. The reaction energy loss estimated using the Tarasov's formula [31] may fluctuate by a few 10% but the magnitude of reaction energy loss was about 1% of fragment kinetic energy; therefore, the uncertainty attributed to reaction energy loss is no more than 1%. The magnitude of energy straggling, estimated using ATIMA [37], ranges from 1.1 to 3.1 MeV/u depending on the fragment species and reaction energy. Uncertainty attributed to energy straggling is the largest (about 2.5%) when primary ions are fragmented near the downstream surface of the target. In the experimental data processing, the measured cross sections were averaged over an energy bin as large as the energy uncertainty.

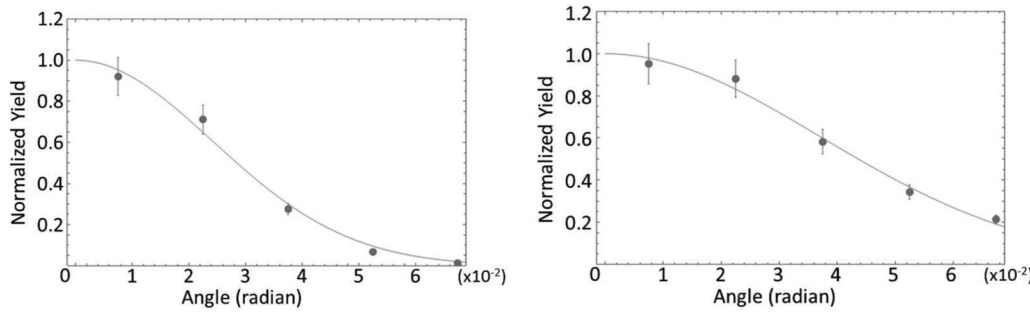

FIG. 5. Angular distribution of fragments produced at 400 MeV/u measured behind target. Closed circles represent measured data, and solid line shows Gaussian fit to data.

Uncertainties of cross sections were estimated considering the following components:

(1) fragment loss by multiple reactions,
(2) detector solid angle,
(3) isotopic identification,
(4) double reaction gain,
(5) acceptance correction,
(6) counting statistical error.

Although fragment loss due to multiple reactions has been evaluated using total reaction cross section parametrization, its uncertainty has not been evaluated in the literature [33]. The uncertainty was estimated to be 10% based on the ^{12}C($^{\mathrm{Nat}}$C,x)X cross section shown in [38]. The uncertainty of reaction loss correction factor calculated based on 10% of the total reaction cross section error is about 3.6%. The 2.67% uncertainty in the detector solid angle arises from the detector dimensions. The uncertainty originating from isotopic identification was estimated by dividing the data points twice, and the fluctuation in the number of data points was evaluated. Double-reaction gain refers to the contribution of fragments produced by more than one reaction inside the target. This component was estimated based on the fragmentation cross section calculated using EPAX [39] and stopping power calculated using SRIM. It can be uncertain owing to error in the production cross section calculated using EPAX, the error of which is estimated to be 10% according to the literature [39]. The uncertainty in acceptance correction originates from the finiteness of detector acceptance. This uncertainty component was evaluated as an error in the angular distribution extrapolation. The counting statistical error was estimated from the number of events in each data point.

B. Model description

The measured cross section data were used to benchmark the nuclear reaction models implemented in the Particle and Heavy Ion Transport code System (PHITS) [27]. In PHITS, nucleus-nucleus reactions were simulated by combining the dynamic nucleus-nucleus reaction model JQMD [40] and the statistical decay Generalized Evaporation Model (GEM) [41]. In addition to the framework based on the QMD approach [10], JQMD is featured by the following assumptions. In nuclei before collision, nucleons are packed within a radius proportional to the $1/3$ power of mass number, and the momenta of the nucleons were sampled randomly within the local Fermi momentum. Before collision, the nuclear ground state thus configured was heated/cooled by introducing frictional force between nucleons and letting nucleons undergo time evolution (hereafter, frictional heating/cooling) until the binding energy agreed with the empirically known binding energy tabulated for GEM. The projectile and target in their respective ground states were located according to a randomly sampled impact parameter and collided considering classical Coulomb trajectory. The strong repulsive forces between nucleons close to each other were treated as stochastic two-body collisions, whereas the soft interaction between remote nucleons was treated as a potential term of the Hamiltonian. The cross sections of two-body collisions were calculated using the modified Cugnon's parametrization [42,43]. The potential term of Hamiltonian was calculated as a sum of Skyrme-type force terms, a Coulomb interaction term, and a symmetry term:

$$V_i = \frac{1}{2}\frac{A}{\rho_s}\langle\rho_i\rangle + \frac{1}{1+\tau}\frac{B}{\rho_s^{\tau}}\langle\rho_i\rangle^{\tau} + \frac{1}{2}\sum_j \frac{c_i c_j\, e^2}{|\mathbf{R_i}-\mathbf{R_j}|} \times \mathrm{erf}\left(\frac{|\mathbf{R_i}-\mathbf{R_j}|}{\sqrt{4L}}\right) + \frac{C_s}{2\rho_s}\sum_j (1-2|c_i-c_j|)\rho_{ij}, \quad (6)$$

where V_i is the potential of the ith nucleon, A is a Skyrme force parameter ($= -219.4$ MeV), ρ_s is the saturation density ($= 0.168$ fm^{-3}), $\langle\rho_i\rangle$ is the overlap integral of wave packets between the ith nucleon and all the other nucleons, B is another Skyrme force parameter ($= 165.3$ MeV), τ is 4/3, c_i is 1 for protons and 0 for neutrons, e is the elementary charge, $\mathbf{R_i}$ denotes the position of ith nucleon, L is the width of wave packet representing nucleons ($= 2$ fm^2), C_s is the symmetry energy parameter ($= 25$ MeV), and ρ_{ij} is the overlap integral of wave functions of the ith and jth nucleons. The first two, third, and fourth terms are Skyrme-type terms, the Coulomb term, and symmetry term, respectively.

After 150 fm/c of time evolution, the spatial coordinates and momenta of nucleons in the phase space were checked cyclopedically and nucleon pairs closer than 4 fm and relative momentum smaller than the local Fermi momentum were bound. Excitation energy and momentum of the fragments were calculated by summing the corresponding value of clustered nucleons. Because the time evolution was simulated in 150 steps of 1-fm/c-long time evolution, energy and momentum conservation was violated slightly owing to the error in numerical integration; therefore, total energy was calculated at the end of 150-fm/c-long time evolution, and the total energy was balanced by scaling the excitation energy of the clusters. The scaling correction was generally smaller than a few 10%. Additional details on JQMD are available in the original article [40].

When applying JQMD to the analysis of nucleus-nucleus fragmentation, the problem was inaccurate treatment of peripheral collisions. It has been suggested that PHITS underestimates fragmentation, losing a small number of nucleons that are produced mostly by peripheral collisions (see [44] for example). The inaccuracy of JQMD for peripheral collision simulation was attributed to spurious excitation and disintegration of nuclei during time evolution. Such spurious excitation and disintegration could not be distinguished from the true ones caused by peripheral collisions. Therefore to inhibit spurious reactions, ground-state nuclei were stabilized by revising the Hamiltonian considering relativistic covariance.

In JQMD, the formalism of dynamics was not relativistically covariant, which means that the time evolution of nucleons depended on the frame of reference. Therefore, nucleons in the ground-state nuclei, steadily bound in the rest frame, often strayed out of their steady states during time evolution in the reaction center-of-mass frame. Once dynamics was described in a relativistically covariant form, spurious disintegration induced by the reference frame transformation was suppressed. In JQMD, the equations of motion for

nucleons were written as follows:

$$\dot{\mathbf{r}}_\mathbf{i} = \frac{\mathbf{p_i}}{m} + \frac{\partial\langle\hat{V}\rangle}{\partial\mathbf{p_i}}, \qquad \dot{\mathbf{p}}_\mathbf{i} = -\frac{\partial\langle\hat{V}\rangle}{\partial\mathbf{r_i}}, \tag{7}$$

where $\mathbf{r_i}$ is the spatial coordinate of the centroid of the ith nucleon, $\mathbf{p_i}$ is the momentum of the ith nucleon, m is the rest mass of nucleons, and $\langle\hat{V}\rangle$ is the potential summed over all nucleons. In both JQMD and JQMD-2.0, the potential term of the Hamiltonian V is a sum of the Skyrme-type force term, Coulomb interaction term, and symmetry term, as explained above.

In contrast, Mancusi *et al.* revised the formulation to consider relativistic covariance [30] of the Hamiltonian. The revised equation of motion is as follows:

$$\dot{\mathbf{r}}_\mathbf{i} = \frac{\mathbf{p_i}}{2p_i^0} + \sum_j^N \frac{m}{p_j^0}\frac{\partial\langle\hat{V}_j\rangle}{\partial\mathbf{p_i}}, \qquad \dot{\mathbf{p}}_\mathbf{i} = -\sum_j^N \frac{m}{p_j^0}\frac{\partial\langle\hat{V}_j\rangle}{\partial\mathbf{r_i}}, \qquad p_i^0 = \sqrt{\mathbf{p_i}^2 + m^2 + 2m\langle\hat{V}_i\rangle}, \tag{8}$$

where $\langle\hat{V}_j\rangle$ is the potential of jth particle, and N is the number of particles in the system. Additional details are provided in the original article. In the JQMD-2.0 developed in this study, the above equation of motion was adopted.

In addition to nuclear ground-state stability, nuclear medium effect near the nuclear surface was modified for accurate simulation of peripheral collisions. The neutron-proton scattering cross section was always suppressed by Pauli blocking in JQMD regardless of the nuclear density, local Fermi momentum, or impact parameter. This assumption is not reasonable for scattering near the nuclear surface, where Pauli blocking is weak and, thereby, the cross section should be close to that in free space. In the revised version, when the impact parameter is larger than 60% of the maximum impact parameter (its definition is explained later), the cross section in free space is adopted because scattering occurs only near the nuclear surface. Meanwhile, when the impact parameter is smaller than 60% of the maximum impact parameter, the cross section suppressed by Pauli blocking is adopted because it is likely that scattering occurs inside dense nuclear matter. For neutron-neutron and proton-proton scattering, cross sections in free space were adopted both in JQMD and JQMD-2.0 because these cross sections are already small, which renders negligible the effect of cross section suppression in central collisions. Here, the maximum impact parameter was determined in advance by simulating collisions in which the impact parameter was swept. The impact parameter at points with inelastic reaction probability lower than 20% during the impact-parameter sweep from zero was regarded as the maximum impact parameter.

In addition to the above-mentioned modifications to physical mechanisms, a few technical approximations adopted in JQMD to suppress spurious disintegration and excitation were revised. Lorentz covariance of kinematics is important not only for the reaction phase but also for the frictional cooling/heating phase. In JQMD, the ground state adjusted in the nucleus rest frame became unstable in the center-of-mass frame; therefore, frictional cooling/heating was performed in the center-of-mass frame. Owing to the Lorentz noncovariant kinematics in JQMD, the nucleon configuration was diffused through the frictional cooling/heating. In JQMD-2.0, by contrast, nuclear stability is independent of the frame of reference; therefore, the nuclei are heated/cooled in the rest frame without being distorted.

Despite the stabilization of nuclei, the nuclei occasionally disintegrated before collisions because QMD could not configure nucleons in the true ground state by its concept. JQMD-2.0 arranges nucleons in $6N$-dimensional phase space randomly and slightly rearranges nucleons by frictional cooling/heating. Because the resulting nucleon configurations are approximate "ground states," a few of them are spuriously excited or disintegrated during the time evolution. Such unstable ground states are excluded before being used as the reaction initial setup. For each nucleon configuration, time evolution is followed for a time scale of 150 fm/c, which is the typical time interval required to simulate a nuclear collision. After the time evolution, the configuration is accepted as the ground state if no nucleons are dropped and the following condition is satisfied:

$$E_{\mathrm{ex}} < \min(S_{\mathrm{n}}, S_{\mathrm{p}} + V_{\mathrm{p}}, S_\alpha + V_\alpha), \tag{9}$$

where E_{ex} is the nucleus excitation energy, S_{n} is the neutron separation energy, S_{p} is the proton separation energy, S_α is the alpha particle separation energy, V_{p} is the Coulomb barrier for proton emission, and V_α is the Coulomb barrier for alpha particle emission. The Coulomb barrier is calculated in the same way as in the downstream evaporation model GEM [41]. This stability test is performed when the impact parameter is larger than $(b_{\max} - 4)$ fm because nuclei likely undergo violent interactions in more central collisions, in which precise stability is unimportant. Because ground-state nuclei were unstable in JQMD, the impact parameter was intentionally limited to cut off spurious decay in noncollision events. In JQMD-2.0, nuclei do not decay in noncollision events, so the impact parameter sampling range is extended as far as inelastic interactions occur.

Furthermore, elasticity judgment in JQMD-2.0 has been modified. To conserve the total reaction probability, which is important to analyze the attenuation of the primary ion beam in thick targets, the inelastic reaction cross section is calculated using the Kurotama model [33]. In accordance with the fact that nucleus-nucleus collisions are simulated when the inelastic reaction probability is sampled, reaction simulation must be reattempted by resampling the impact parameter if the simulated reaction was elastic. When the dynamic phase of a reaction is simulated using JQMD-2.0, the run is either elastic, inelastic, or non-energy-conserving depending on the final state. In elastic runs, no nucleons are dropped, and the excitation energies of both the projectile and target are lower than the evaporation threshold. The evaporation threshold is

calculated according to Eq. (10) in JQMD:

$$E_{\mathrm{ex}} < 0.3 \times A \ \mathrm{MeV},$$

where A is the mass number, whereas the more precise condition given by Eq. (9) is used in JQMD-2.0. In both JQMD and JQMD-2.0, elastic runs were rejected and simulation was started afresh with resampling of the impact parameter. In inelastic runs, any nucleons were dropped or the excitation energies of projectile or target were higher than the evaporation threshold. In addition, the total energy at the end of the run can be balanced by scaling the excitation energy of nuclei. If the total energy cannot be balanced by adjusting the excitation energy (i.e., total energy exceeds the available energy) the runs are categorized as non-energy-conserving runs. The inelastic runs were scored as successful events, whereas the non-energy-conserving runs were rejected and restarted in both JQMD and JQMD-2.0; however, in the non-energy-conserving runs, the impact parameter was sampled afresh in JQMD whereas the same impact parameter was used in JQMD-2.0. According to the scheme adopted in JQMD, central collision runs were often rejected as non-energy-conserving runs; therefore, the impact parameter distribution was biased (i.e., reactions seldom occurred at small impact parameters).

III. RESULTS AND DISCUSSION

A. Fragmentation cross sections

The cross sections measured in our experiment are compared with the literature data (Webber [45] at 600 MeV/u, Yashima [4] at 100, 230, and 400 MeV/u, and Kidd [46] at 250 MeV/u), EPAX, and calculation by JQMD and JQMD-2.0 in Figs 6–13. The horizontal distance between the experimental data points corresponds to energy uncertainty. Because EPAX assumes that the cross section is energy independent in the intermediate energy range, the cross sections calculated using EPAX were plotted as horizontal lines. Our measurement agrees with the literature data within 20%, except for the ^{11}B and ^{7}Be production cross section measured by Yashima at 400 MeV/u. In Fig. 10, the data points of Webber and EPAX indicate that the cross section is about 20 mb or less; therefore, Yashima's data

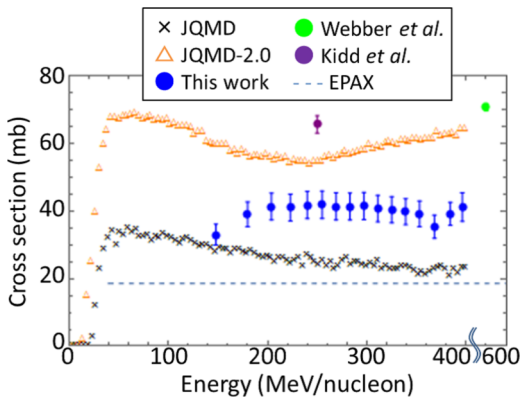

FIG. 6. (Color online) ^{12}C($^{\mathrm{Nat}}$C, X)^{11}B cross sections. △: Calculation by PHITS-JQMD-2.0; ×: Calculation by PHITS-JQMD; blue filled circles: measurement in this experiment; the circles filled with other colors denote literature data.

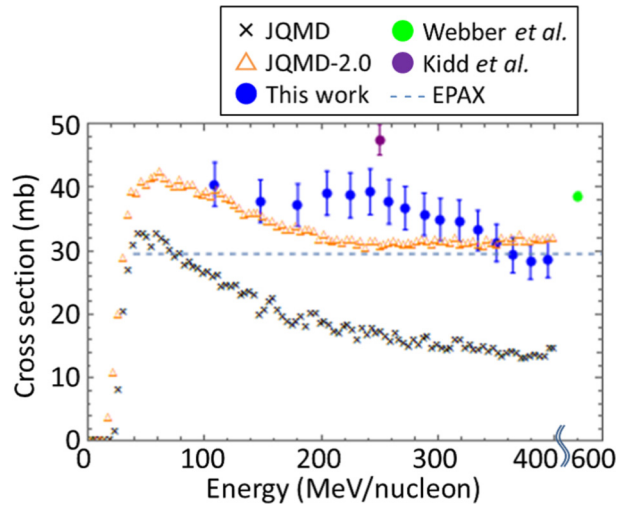

FIG. 7. (Color online) ^{12}C($^{\mathrm{Nat}}$C, X)^{10}B cross sections.

may include unevaluated uncertainties, and our data are more consistent with the other data. Our experimental data indicate that the cross sections decrease with increasing incident energy. This trend, particularly pronounced for light nuclei, is attributed to the fact that a greater number of collisions is necessary to produce lighter nuclei, and nucleon-nucleon cross sections decrease with increasing energy. A similar declining trend was observed in charge-changing cross sections measured by Yamaguchi [5] in the energy range up to 300 MeV/u. Partial charge-changing cross section parametrization using Sihver's formula suggests that B production cross section is rather energy independent, whereas Li production decreases with increasing energy. Moreover, the energy dependence obtained in our experiment is consistent with the total reaction cross section systematics [33,38,47]. Analysis of total reaction cross section energy dependence using the Glauber theory [48] also suggests that cross sections decrease with increasing energy. All these facts support the energy-dependent trend of cross sections obtained in our experiment, which indicates that we succeeded in measuring the isotopic fragmentation cross sections as functions of energy by using the method developed in this study.

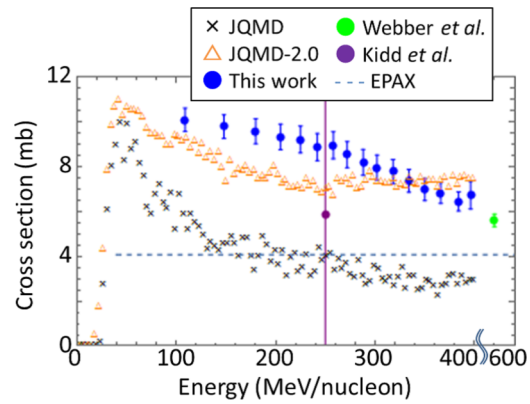

FIG. 8. (Color online) ^{12}C($^{\mathrm{Nat}}$C, X)^{10}Be cross sections.

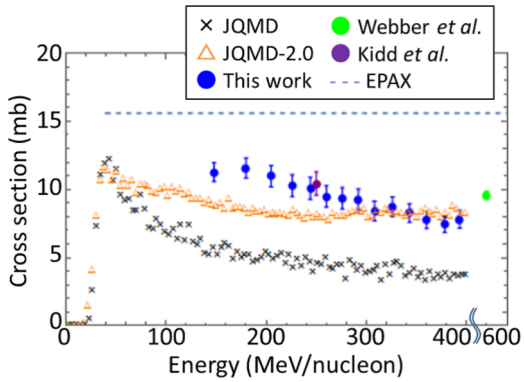

FIG. 9. (Color online) ^{12}C($^{\mathrm{Nat}}$C, X)^{9}Be cross sections.

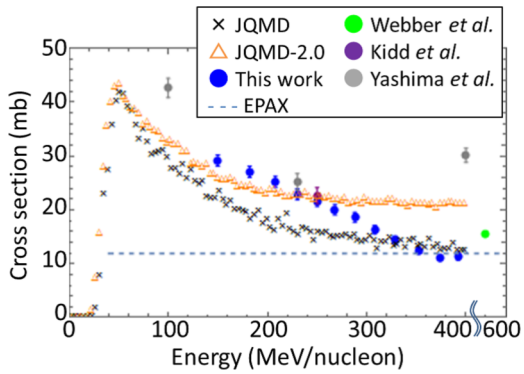

FIG. 10. (Color online) ^{12}C($^{\mathrm{Nat}}$C, X)^{7}Be cross sections.

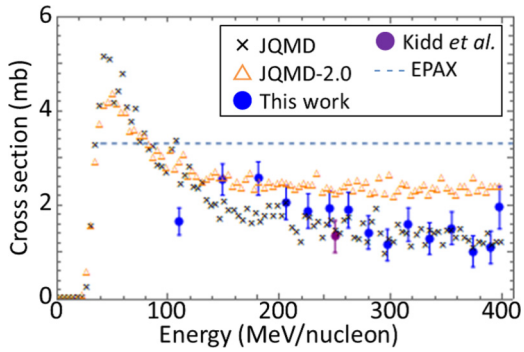

FIG. 11. (Color online) ^{12}C($^{\mathrm{Nat}}$C, X)^{8}Li cross sections.

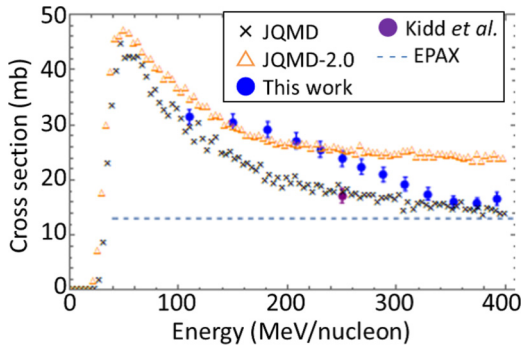

FIG. 12. (Color online) ^{12}C($^{\mathrm{Nat}}$C, X)^{7}Li cross sections.

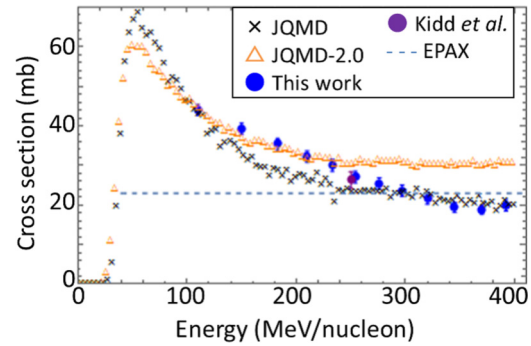

FIG. 13. (Color online) ^{12}C($^{\mathrm{Nat}}$C, X)^{6}Li cross sections.

The production cross sections for heavy fragments, i.e., ^{10}B, ^{10}Be and ^{9}Be, calculated by JQMD-2.0 agree with the experimental data better than those calculated with JQMD do. This is attributed to the impact parameter limitation in JQMD. In the case of carbon-carbon reactions, the impact parameter was sampled below 4.86 fm in JQMD, which is smaller than twice the carbon nuclear radius. Owing to this impact parameter limitation, a large portion of nuclei was often involved in reactions and eventually disrupted. JQMD-2.0, in contrast, allows for reactions at large impact parameters, which tend to produce heavy fragments such as ^{10}B, ^{10}Be, and ^{9}Be.

Furthermore, when nuclei underwent soft collisions without knocking out nucleons, the event was accepted as an inelastic reaction if the excitation energy was larger than 0.3A MeV in JQMD. In the case of ^{12}C, the value (3.6 MeV) was too small to regard the reaction as inelastic because at least 7.37 MeV of excitation energy is required to cause inelastic reactions. This means that JQMD unreasonably accepted some elastic reactions with excitation energies between 3.6 and 7.37 MeV as inelastic reactions, resulting in the underestimation of fragment yield.

For nuclei lighter than 8 amu, both JQMD and JQMD-2.0 agree fairly well with the measured data. In the simulation, a large portion of nuclei lighter than 8 amu were produced by scratching a few nucleons followed by the evaporation of a single alpha particle (e.g., ^{7}Be was produced by knocking out one neutron in the dynamic phase and evaporating one alpha particle), whereas the production of nuclei heavier than 8 amu did not involve alpha particle emission. This fact indicates an important aspect of near-projectile fragment

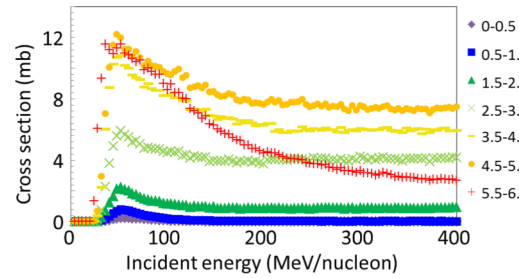

FIG. 14. (Color online) Contribution to ^{7}Be production in ^{12}C($^{\mathrm{Nat}}$C,x) reactions from different impact parameter ranges as simulated using JQMD-2.0.

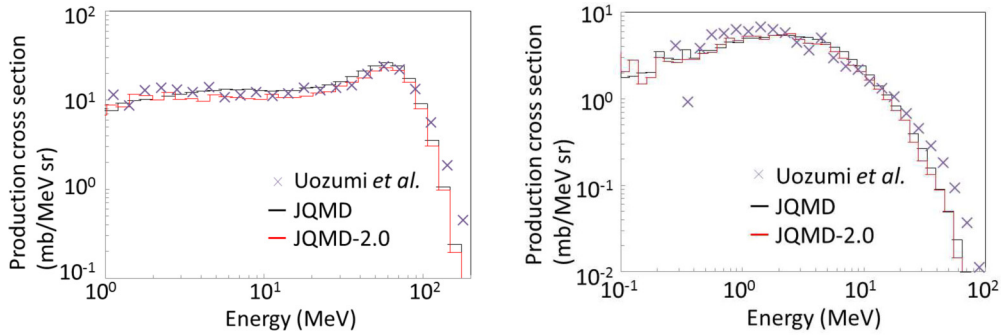

(a) 15 degrees (b) 90 degrees

FIG. 15. (Color online) Double-differential neutron production cross sections of 100 MeV/u ^{12}C(^{Nat}C,x) reactions calculated by JQMD, JQMD-2.0, and literature data [49].

production. To produce heavy fragments, it is important to knock out a few nucleons without being substantially excited. In the dynamic phase of peripheral collisions, nucleons in shallow potential near the nuclear surface are taken away; therefore, the nuclei are only slightly excited. Using the smeared ground-state nuclei configured by JQMD, which have a noticeable low-density near-surface region, the production of heavy nuclei is overestimated if the impact parameter range is extended outward. JQMD agreed with the experimental data by compensating for the two effects: ground state smearing and impact parameter limitation. The generation of a reasonable ground-state configuration and unrestricted impact parameter sampling by JQMD-2.0 is crucial for the accurate treatment of peripheral collisions.

The use of free-nucleon cross sections is important for fragment production. Using Pauli-suppressed cross sections even above 60% of the maximum impact parameter, nucleon-nucleon scattering is suppressed; therefore, fewer fragments are produced. In Fig. 14, the correlation between nucleon-nucleon scattering cross section and ^{7}Be yield is shown clearly as the partial yield in the 5.5–6.5 fm range. Production decreased with increase in energy, which corresponds to decreased nucleon-nucleon scattering cross sections. It is also shown that fragment production (^{7}Be in the case of Fig. 14) is mainly attributed to reactions whose impact parameter is larger than 3.5 fm, and the nucleon-nucleon scattering cross section is suppressed only below 3.8–4.8 fm (60% of the maximum impact parameter). If the cross sections are suppressed even at larger impact parameters, as in JQMD, ^{7}Be production would decrease owing to a decrease in nucleon-nucleon scattering. This trend is commonly seen in the other measured fragments.

B. Neutron production cross sections

Secondary particle yields and residue production are complementary aspects of nuclear fragmentation. Neutron production cross sections in carbon-carbon reactions are compared in Figs. 15 and 16. In Fig. 15, neutron yields in ^{12}C(^{Nat}C,x)X reactions by 100 MeV/u ^{12}C calculated using JQMD and JQMD-2.0 differ by less than 20%, which is not larger than the fluctuation in experimental data. At large emission angles, the difference is negligible at both 100 and 290 MeV/u, as shown in Figs. 15(b) and 16(b). Figure 16 (a) shows that the neutron yield calculated with JQMD-2.0 is lower than that calculated with JQMD by 30%. Consequently, the result of JQMD-2.0 agrees well with the experimental data at the high-energy peak, whereas neutron yield is insufficient in the 20–10 MeV energy region. However, the experimental data shown in Fig. 17, almost equivalent to those in Fig. 16(a), agree well with the calculation result obtained using JQMD-2.0 in

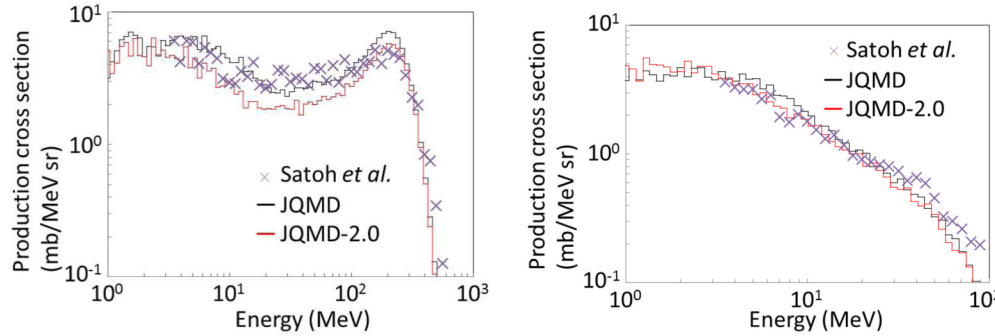

(a)15 degrees (b)90 degrees

FIG. 16. (Color online) Double-differential neutron production cross sections of 290 MeV/u ^{12}C(^{Nat}C,x) reactions calculated using JQMD, JQMD-2.0, and literature data [50].

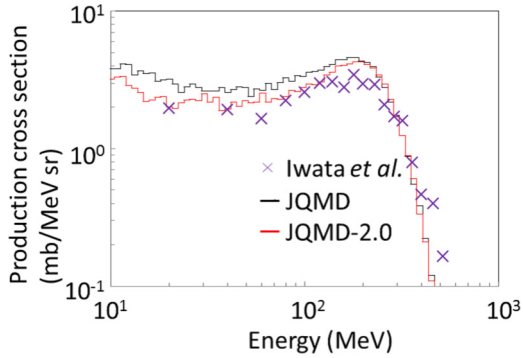

FIG. 17. (Color online) Double-differential neutron production cross sections of 290 MeV/u ^{12}C($^{\mathrm{Nat}}$C,x) reactions at 20 degrees calculated using JQMD, JQMD-2.0, and literature data [51].

the 20–100 MeV energy region. This fact suggests that the neutron yields calculated using JQMD-2.0 agree within the fluctuations among experimental data.

As shown in Figs. 15 and 16, the neutron production calculated using JQMD-2.0 is mostly similar to that calculated using JQMD. Figure 18 shows the partial neutron double-differential cross sections calculated by sweeping the impact parameter. It shows that neutron yield is abundant in the impact parameter range of 1–4 fm, and this trend is true for JQMD as well, though it is not shown in the figure. Therefore, restricting the impact parameter range below 4.86 fm under the fixation of the inelastic reaction cross section led to increased neutron yield. In contrast, impact parameter resampling in the non-energy-conserving runs in JQMD reduced reactions at small impact parameters, which resulted in decreased neutron yield. The agreement between experimental data and JQMD results indicates that these two effects are compensated. In a similar way as the fragment yield discussed above, the revised procedure adopted in JQMD-2.0 is more reasonable for simulating neutron yields.

IV. CONCLUSION

The fragment production excitation functions of ^{12}C($^{\mathrm{Nat}}$C,x)X reactions were measured following a new method that uses a thick target and a telescope detector. Using the new method, the energy dependence of isotopic fragment production cross sections was obtained successfully by identifying fragment mass and charge. The consistency of the measured cross sections and literature data indicates the validity of our measurement. The measured cross sections generally exhibit energy-dependent decline, and the decline is more pronounced for lighter products.

JQMD was then revised to accurately reproduce the measured production of fragments, particularly heavy fragments produced by peripheral collisions. By revising the description of peripheral collisions, unreasonable assumptions adopted to suppress spurious reactions became unnecessary, and these were therefore excluded from the model. The revision eventually affected the simulation of central collisions and peripheral collisions. Consequently, the revised QMD reproduces the measured fragmentation cross sections generally within a few 10% without degrading the accuracy of secondary particle production simulation.

ACKNOWLEDGMENTS

We wish to thank Dr. Davide Mancusi for providing the source code of the previous version of R-JQMD. We express gratitude to Dr. T. Murakami and the technical staff of NIRS-HIMAC for operating the HIMAC. This work was performed as a Research Project with heavy ions at NIRS-HIMAC. We also thank the operation team of the Center for Computational Science and E-systems (CCSE) in the Japan Atomic Energy Agency. Monte Carlo simulations reported in this paper were executed on a PC-cluster system of CCSE. This work was supported by JSPS KAKENHI Grants No. 24860072 (Grant-in-Aid for Research Activity Start-up), and No. 26790072 (Grant-in-Aid for Young Scientists).

APPENDIX: MEASURED CROSS SECTION DATA

Tables I, II, and III show measured cross section data for ^{12}C(C,x)^{11,10}B, ^{12}C(C,x)^{10,9,7}Be, and ^{12}C(C,x)^{8,7,6}Li, respectively.

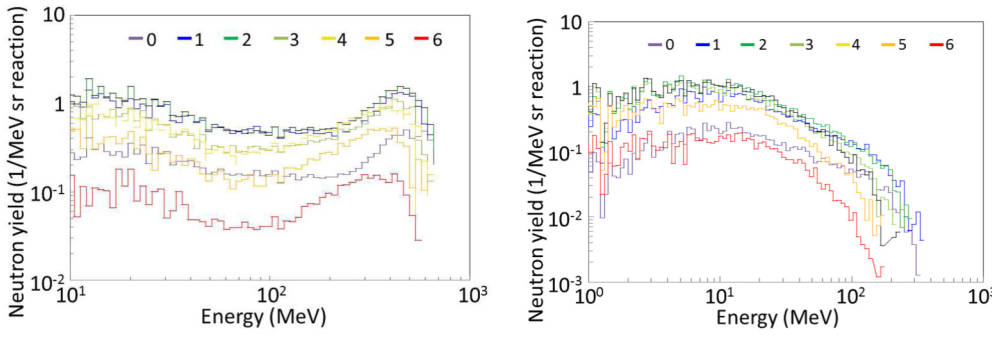

(a) 15 degrees (b) 90 degrees

FIG. 18. (Color online) Contribution to neutron production double-differential cross sections in ^{12}C($^{\mathrm{Nat}}$C,x) reactions by 290 MeV/u ^{12}C from different impact parameter ranges in simulation using JQMD-2.0.

TABLE I. Measured ^{12}C(C,x)^{11,10}B cross sections.

^{11}B		^{10}B	
Energy (MeV/nucleon)	Cross section (mb)	Energy (MeV/nucleon)	Cross section (mb)
148	33.0 ± 3.1	109	40.5 ± 3.4
180	39.0 ± 3.7	148	37.8 ± 3.3
204	41.3 ± 3.9	180	37.2 ± 3.3
223	41.0 ± 3.9	205	39.1 ± 3.5
240	41.8 ± 4.0	225	38.7 ± 3.5
255	41.9 ± 4.1	242	39.3 ± 3.6
269	41.3 ± 4.0	258	37.7 ± 3.5
283	41.3 ± 4.0	272	36.7 ± 3.4
297	41.5 ± 4.0	288	35.8 ± 3.3
311	40.7 ± 3.9	302	34.9 ± 3.3
325	40.3 ± 3.9	318	34.7 ± 3.2
339	39.8 ± 3.8	334	33.2 ± 3.1
353	39.2 ± 3.8	350	31.2 ± 3.0
368	35.3 ± 3.4	364	29.3 ± 2.8
384	39.2 ± 3.4	379	28.3 ± 2.7
396	41.1 ± 4.2	394	28.5 ± 2.9

TABLE II. Measured ^{12}C(C,x)^{10,9,7}Be cross sections.

^{10}Be		^{9}Be		^{7}Be	
Energy (MeV/nucleon)	Cross section (mb)	Energy (MeV/nucleon)	Cross section (mb)	Energy (MeV/nucleon)	Cross section (mb)
109	10.08 ± 0.52	148	11.27 ± 0.69	150	29.1 ± 1.0
148	9.78 ± 0.53	180	11.58 ± 0.74	182	27.0 ± 1.1
180	9.58 ± 0.56	205	10.97 ± 0.78	208	25.2 ± 1.1
205	9.32 ± 0.57	226	10.30 ± 0.79	230	22.9 ± 1.0
225	9.21 ± 0.60	244	10.09 ± 0.80	250	21.6 ± 1.0
242	8.86 ± 0.60	260	9.48 ± 0.79	268	20.0 ± 0.9
258	8.95 ± 0.60	276	9.35 ± 0.79	288	18.7 ± 0.9
272	8.52 ± 0.58	292	9.27 ± 0.77	308	16.3 ± 0.8
288	8.18 ± 0.57	308	8.43 ± 0.72	329	14.4 ± 0.7
302	7.96 ± 0.56	326	8.75 ± 0.72	352	12.5 ± 0.7
318	7.77 ± 0.54	343	8.28 ± 0.68	374	11.2 ± 0.6
334	7.36 ± 0.51	360	7.78 ± 0.64	392	11.3 ± 0.7
350	6.98 ± 0.49	378	7.52 ± 0.58		
366	6.83 ± 0.47	393	7.62 ± 0.66		
384	6.52 ± 0.43				
396	6.59 ± 0.62				

TABLE III. Measured ^{12}C(C,x)^{8,7,6}Li cross sections.

^{8}Li		^{7}Li		^{6}Li	
Energy (MeV/nucleon)	Cross section (mb)	Energy (MeV/nucleon)	Cross section (mb)	Energy (MeV/nucleon)	Cross section (mb)
110	1.65 ± 0.29	110	31.43 ± 1.31	110	44.08 ± 1.32
149	2.54 ± 0.33	150	30.54 ± 1.39	150	39.34 ± 1.37
181	2.56 ± 0.36	182	29.14 ± 1.44	183	35.46 ± 1.42
206	2.05 ± 0.36	208	27.13 ± 1.45	210	32.26 ± 1.46
226	1.87 ± 0.36	230	25.56 ± 1.45	233	30.08 ± 1.49
245	1.93 ± 0.37	250	23.89 ± 1.41	254	27.08 ± 1.46
262	1.90 ± 0.38	268	22.43 ± 1.37	276	25.41 ± 1.46
280	1.42 ± 0.35	288	20.97 ± 1.31	297	23.68 ± 1.43
297	1.15 ± 0.34	308	19.30 ± 1.23	320	21.58 ± 1.37
316	1.59 ± 0.35	329	17.49 ± 1.13	345	19.47 ± 1.26
335	1.29 ± 0.33	352	16.04 ± 1.05	370	19.13 ± 1.17
355	1.51 ± 0.35	374	15.97 ± 0.98	392	19.39 ± 1.37
374	1.02 ± 0.33	392	16.19 ± 1.17		
390	1.10 ± 0.35				
398	1.95 ± 0.46				

[1] G. Giuliani, H. Zheng, and A. Bonasera, The many facets of the (non-relativistic) nuclear equation of state, Prog. Part. Nucl. Phys. **76**, 116 (2014).

[2] J. Pochodzalla, The search for the liquid-gas phase transition in nuclei, Prog. Part. Nucl. Phys. **39**, 443 (1997).

[3] V. Baran, M. Colonna, V. Greco, and M. Di Toro, Reaction dynamics with exotic nuclei, Phys. Rep. **410**, 335 (2005).

[4] H. Yashima, Y. Uwamino, H. Iwase, H. Sugita, T. Nakamura, S. Ito, and A. Fukumura, Cross sections for the production of residual nuclides by high-energy heavy ions, Nucl. Instrum. Methods Phys. Res. Sect. B **226**, 243 (2004).

[5] T. Yamaguchi, M. Fukuda, S. Fukuda, G. W. Fan, I. Hachiuma, M. Kanazawa, A. Kitagawa, T. Kuboki, M. Lantz, M. Mihara, M. Nagashima, K. Namihira, D. Nishimura, Y. Okuma, T. Ohtsubo, S. Sato, T. Suzuki, M. Takechi, and W. Xu, Energy-dependent charge-changing cross sections and proton distribution of ^{28}Si, Phys. Rev. C **82**, 014609 (2010).

[6] C. Zeitlin, S. Guetersloh, L. Heilbronn, J. Miller, A. Fukumura, Y. Iwata, and T. Murakami, Fragmentation cross sections of 290 and 400 MeV/nucleon ^{12}C beams on elemental targets, Phys. Rev. C **76**, 014911 (2007).

[7] C. Zeitlin, J. Miller, S. Guetersloh, L. Heilbronn, A. Fukumura, Y. Iwata, T. Murakami, S. Blattnig, R. Norman, and S. Mashnik, Fragmentation of ^{14}N, ^{16}O, ^{20}Ne, and ^{24}Mg nuclei at 290 to 1000 MeV/nucleon, Phys. Rev. C **83**, 034909 (2011).

[8] D. P Chowdhury, R Guin, S. K Saha, and M Sudersanan, Excitation functions of heavy ion induced nuclear reactions between ^{16}O ion beam and natural copper: Measurements, analysis and its applicability in TLA study, Nucl. Instrum. Methods Phys. Res. Sec. B **211**, 288 (2003).

[9] T. Ogawa, M. N. Morev, T. Sato, and S. Hashimoto, Analysis of fragmentation excitation functions of lead by carbon ions up to 400 Mev/u, Nucl. Instrum. Methods .Phys. Res. Sect. B **300**, 35 (2013).

[10] J. Aichelin and H. Stocker, Quantum molecular dynamics – A novel approach to N-body correlations in heavy ion collisions, Phys. Lett. B **176**, 14 (1986).

[11] H. Flocard, S. E. Koonin, and M. S. Weiss, Three-dimensional time-dependent Hartree-Fock calculations: Application to ^{16}O + ^{16}O collisions, Phys. Rev. C **17**, 1682 (1978).

[12] S. Roesler, R. Engel, and J. Ranft, The Monte Carlo event generator DPMJET-III, in *Advanced Monte Carlo for Radiation Physics, Particle Transport Simulation and Applications*, edited by A. Kling, F. J. C. Barao, M. Nakagawa, L. Tavora, and P. Vaz (Springer Berlin, 2001), pp. 1033–1038.

[13] A. Ono, H. Horiuchi, T. Maruyama, and A. Ohnishi, Fragment Formation Studied with Antisymmetrized Version of Molecular Dynamics with Two-Nucleon Collisions, Phys. Rev. Lett. **68**, 2898 (1992).

[14] S. Chikazumi, T. Maruyama, S. Chiba, K. Niita, and A. Iwamoto, Quantum molecular dynamics simulation of expanding nuclear matter and nuclear multifragmentation, Phys. Rev. C **63**, 024602 (2001).

[15] N. Wang, Z. Li, and X. Wu, Improved quantum molecular dynamics model and its applications to fusion reaction near barrier, Phys. Rev. C **65**, 064608 (2002).

[16] H. Sorge, Flavor production in Pb(160A GeV) on Pb collisions: Effect of color ropes and hadronic rescattering, Phys. Rev. C **52**, 3291 (1995).

[17] N. S. Amelin, K. K. Gudima, and V. D. Toneev, Ultrarelativistic nucleus-nucleus collisions in dynamical model of independent quark-gluon strings, Sov. J. Nucl. Phys. **51**, 1093 (1990).

[18] N. S. Amelin, V. D. Toneev, K. K. Gudima, and S. Yu. Sivoklokov, Further development of a quark-gluon string model for describing high-energy collisions with a nuclear target, Technical report, Joint Institute for Nuclear Research, Dubna (USSR), Laboratory of Theoretical Physics, 1989 (unpublished).

[19] K. K. Gudima, S. G. Mashnik, and A. J. Sierk, User Manual for the Code LAQGSM, Report No. LA-UR(01)-6804, 2001.

[20] S. Leray, D. Mancusi, P. Kaitaniemi, J. C. David, A. Boudard, B. Braunn, and J. Cugnon, Extension of the Liege Intra Nuclear Cascade model to light ion-induced collisions for medical and space applications, J. Phys. Conf. Ser. **420**, 012065 (2013).

[21] T. T. Böhlen, F. Cerutti, M. P. W. Chin, A. Fasso, A. Ferrari, P. G. Ortega, A. Mairani, P. R. Sala, G. Smirnov, and V. Vlachoudis, The FLUKA code: Developments and challenges for high energy and medical applications, Nucl. Data Sheets **120**, 211 (2014).

[22] A. Ferrari, P. R Sala, A. Fasso, and J. Ranft, *FLUKA: A Multi-Particle Transport Code (Program Version 2005)* (CERN, Geneva, 2005).

[23] T. Goorley, M. James, T. Booth, F. Brown, J. Bull, L. J. Cox, J. Durkee, J. Elson, M. Fensin, R. A. Forster, J. Hendricks, H. G. Hughes, R. Johns, B. Kiedrowski, R. Martz, S. Mashnik, G. McKinney, D. Pelowitz, R. Prael, J. Sweezy, L. Waters, T. Wilcox, and Zukaitis T, Initial MCNP6 release overview, Nucl. Technol. **180**, 298 (2012).

[24] S. Agostinelli, J. Allison, K. Amako, J. Apostolakis, H. Araujo, P. Arce, M. Asai, D. Axen, S. Banerjee, G. Barrand, F. Behner, L. Bellagamba, J. Boudreau, L. Broglia, A. Brunengo, H. Burkhardt, S. Chauvie, J. Chuma, R. Chytracek, G. Cooperman, G. Cosmo, P. Degtyarenko, A. Dell'Acqua, G. Depaola, D. Dietrich, R. Enami, A. Feliciello, C. Ferguson, H. Fesefeldt, G. Folger, F. Foppiano, A. Forti, S. Garelli, S. Giani, R. Giannitrapani, D. Gibin, J. J. Gomez Cadenas, I. Gonzalez, G. Gracia Abril, G. Greeniaus, W. Greiner, V. Grichine, A. Grossheim, S. Guatelli, P. Gumplinger, R. Hamatsu, K. Hashimoto, H. Hasui, A. Heikkinen, A. Howard, V. Ivanchenko, A. Johnson, F. W. Jones, J. Kallenbach, N. Kanaya, M. Kawabata, Y. Kawabata, M. Kawaguti, S. Kelner, P. Kent, A. Kimura, T. Kodama, R. Kokoulin, M. Kossov, H. Kurashige, E. Lamanna, T. Lampen, V. Lara, V. Lefebure, F. Lei, M. Liendl, W. Lockman, F. Longo, S. Magni, M. Maire, E. Medernach, K. Minamimoto, P. Mora de Freitas, Y. Morita, and K. Murakami, Geant4 – A simulation toolkit, Nucl. Instrum. Methods Phys. Res. Sect. A **506**, 250 (2003).

[25] N. Bassler, D. C. Hansen, A. Luhr, B. Thomsen, J. B. Petersen, and N. Sobolevsky, SHIELD-HIT12A – A Monte Carlo particle transport program for ion therapy research, J. Phys. Conf. Ser. **489**, 012004 (2014).

[26] D. C Hansen, A. Luhr, N. Sobolevsky, and N. Bassler, Optimizing SHIELD-HIT for carbon ion treatment, Phys. Med. Biol. **57**, 2393 (2012).

[27] T. Sato, K. Niita, N. Matsuda, S. Hashimoto, Y. Iwamoto, S. Noda, T. Ogawa, H. Iwase, H. Nakashima, T. Fukahori, K. Okumura, T. Kai, S. Chiba, T. Furuta, and L. Sihver, Particle and Heavy Ion Transport code System, PHITS, version 2.52, J. Nucl. Sci. Technol. **50**, 913 (2013).

[28] L. Sihver, D. Mancusi, K. Niita, T. Sato, L. Townsend, C. Farmer, L. Pinsky, A. Ferrari, F. Cerutti, and I. Gomes, Benchmarking of calculated projectile fragmentation cross-sections using the 3-D, MC codes PHITS, FLUKA, HETC-HEDS, MCNPX-HI, and NUCFRG2, Acta Astron. **63**, 865 (2008).

[29] D. Mancusi, L. Sihver, K. Gustafsson, C. La Tessa, S. B. Guetersloh, C. J. Zeitlin, J. Miller, L. H. Heilbronn, K. Niita, T. Sato, H. Nakashima, T. Murakami, and Y. Iwata, PHITS – Benchmark of partial charge-changing cross sections for intermediate-mass systems, Nucl. Instrum. Methods .Phys. Res. Sect. B **254**, 30 (2007).

[30] D. Mancusi, K. Niita, T. Maruyama, and L. Sihver, Stability of nuclei in peripheral collisions in the JAERI quantum molecular dynamics model, Phys. Rev. C **79**, 014614 (2009).

[31] O. Tarasov, Analysis of momentum distributions of projectile fragmentation products, in *Proceedings of the Eighth International Conference On Nucleus-Nucleus Collisions* [Nucl. Phys. A **734**, 536 (2004)].

[32] J. F. Ziegler, M. D. Ziegler, and J. P. Biersack, SRIM – The stopping and range of ions in matter, in 19th International Conference on Ion Beam Analysis [Nucl. Instrum. Methods Phys. Res. Sect. B **268**, 1818 (2010)].

[33] L. Sihver, A. Kohama, K. Iida, K. Oyamatsu, S. Hashimoto, H. Iwase, and K. Niita, Current status of the hybrid Kurotama model for total reaction cross sections, Nucl. Instrum. Methods .Phys. Res. Sect. B **334**, 34 (2014).

[34] K. Omata, Y. Fujita, N. Yoshikawa, M. Sekiguchi, and Y. Shida, A data acquisition system based on a personal computer, IEEE Trans. Nucl. Sci. **39**, 143 (1992).

[35] G. R. Lynch and O. I. Dahl, Approximations to multiple coulomb scattering, Nucl. Instrum. Methods Phys. Res. Sect. B **58**, 6 (1991).

[36] A. S. Goldhaber, Statistical models of fragmentation processes, Phys. Lett. B **53**, 306 (1974).

[37] https://web-docs.gsi.de/∼weick/atima/

[38] R. K. Tripathi, F. A. Cucinotta, and J. W. Wilson, Accurate universal parametrization of absorption cross sections, Nucl. Instrum. Methods Phys. Res. Sect. B **117**, 347 (1996).

[39] K. Summerer and B. Blank, EPAX version 2: A modified empirical parametrization of fragmentation cross sections, in 5th International Conference on Radioactive Nuclear Beams [Nucl. Phys. A **701**, 161 (2002)].

[40] K. Niita, S. Chiba, T. Maruyama, T. Maruyama, H. Takada, T. Fukahori, Y. Nakahara, and A. Iwamoto, Analysis of the (N,xN') reactions by quantum molecular dynamics plus statistical decay model, Phys. Rev. C **52**, 2620 (1995).

[41] S. Furihata, Statistical analysis of light fragment production from medium energy proton-induced reactions, Nucl. Instrum. Methods Phys. Res. Sect. B **171**, 251 (2000).

[42] J. Cugnon, T. Mizutani, and J. Vandermeulen, Equilibration in relativistic nuclear collisions. A Monte Carlo calculation, Nucl. Phys. A **352**, 505 (1981).

[43] J. Cugnon, Monte Carlo calculation of high-energy heavy-ion interactions, Phys. Rev. C **22**, 1885 (1980).

[44] H. Rohling, L. Sihver, M. Priegnitz, W. Enghardt, and F. Fiedler, Comparison of PHITS, GEANT4, and HIBRAC simulations of depth-dependent yields of β^{+-} emitting nuclei during therapeutic particle irradiation to measured data, Phys. Med. Biol. **58**, 6355 (2013).

[45] W. R. Webber, J. C. Kish, and D. A. Schrier, Individual isotopic fragmentation cross sections of relativistic nuclei in hydrogen, helium, and carbon targets, Phys. Rev. C **41**, 547 (1990).

[46] J. M. Kidd, P. J. Lindstrom, H. J. Crawford, and G. Woods, Fragmentation of carbon ions at 250 Mev/nucleon, Phys. Rev. C **37**, 2613 (1988).

[47] S. Kox, A. Gamp, C. Perrin, J. Arvieux, R. Bertholet, J. F. Bruandet, M. Buenerd, R. Cherkaoui, A. J. Cole, Y. El-Masri, N. Longequeue, J. Menet, F. Merchez, and J. B. Viano, Trends of total reaction cross sections for heavy ion collisions in the intermediate energy range, Phys. Rev. C **35**, 1678 (1987).

[48] M. Takechi, M. Fukuda, M. Mihara, K. Tanaka, T. Chinda, T. Matsumasa, M. Nishimoto, R. Matsumiya, Y. Nakashima, H. Matsubara, K. Matsuta, T. Minamisono, T. Ohtsubo, T. Izumikawa, S. Momota, T. Suzuki, T. Yamaguchi, R. Koyama, W. Shinozaki, M. Takahashi, A. Takizawa, T. Matsuyama, S. Nakajima, K. Kobayashi, M. Hosoi, T. Suda, M. Sasaki, S. Sato, M. Kanazawa, and A. Kitagawa, Reaction cross sections at intermediate energies and Fermi-motion effect, Phys. Rev. C **79**, 061601 (2009).

[49] Y. Uozumi, Y. Itashiki, D. Satoh, T. Kajimoto, T. Sanami, Y. Koba, M. Takada, N. Matsufuji, Y. Imahayashi, and N. Shigyo, Measurement of cross sections and yield of neutron produced by 100 MeV/u C(C,xn) reaction, Report No. JAEA-Conf 2014-002 (unpublished).

[50] D. Satoh (private communication).

[51] D. Satoh, D. Moriguchi, T. Kajimoto, Y. Koba, Y. Nakamura, N. Shigyo, M. Ueyama, Y. Uozumi, and M. Yoshioka, Neutron-production double-differential cross sections from heavy-ion interactions, J. Korean Phys. Soc. **59**, 1741 (2011).